Estuarine, Coastal and Shelf Science 298 (2024) 108654

Contents lists available at ScienceDirect

Estuarine, Coastal and Shelf Science

journal homepage: www.elsevier.com/locate/ecss

Salt intrusion and effective longitudinal dispersion in man-made canals, a simplified model approach

Bouke Biemond [a,*], Vincent Vuik [b], Paula Lambregts [b], Huib E. de Swart [a], Henk A. Dijkstra [a]

[a] Department of Physics, Institute for Marine and Atmospheric Research Utrecht, Utrecht University, Utrecht, The Netherlands
[b] HKV Lijn in water B.V., Lelystad, The Netherlands

ARTICLE INFO

Keywords:
Salt intrusion
Idealized modeling
Dispersion parametrization
Ghent-Terneuzen Canal
Freshwater management

ABSTRACT

Salinization threatens coastal freshwater bodies, but little is known about this phenomenon in man-made canals. Here, salt intrusion and effective longitudinal dispersion in such canals are investigated, where the Ghent-Terneuzen Canal in Belgium-the Netherlands is used as a prototype example. A calibrated, width-averaged model is employed to quantify the sensitivity of these quantities to forcing conditions. This model performs better than a calibrated, cross-sectionally averaged model with a constant longitudinal dispersion coefficient, because density-driven advection of salt, which turns out to be important in man-made canals, is explicitly resolved. It is found that, in equilibrium, discharge at the upstream boundary is more important than exterior salinity for salt intrusion and effective longitudinal dispersion. Furthermore, the time-dependent salinity response to an increase in freshwater discharge is faster than that to a decrease in discharge. In contrast, the time it takes the system to adjust to a change in the exterior salinity does not depend on the sign of that change. From these results, a parametrization of the effective longitudinal dispersion coefficient is developed, which explicitly accounts for the horizontal salt transport by the density-driven current. A cross-sectionally averaged model that uses this effective longitudinal dispersion coefficient successfully simulates the salt dynamics of the width-averaged model.

1. Introduction

Many coastal regions all over the world are facing increases in salt intrusion (Eslami et al., 2021; Bellafiore et al., 2021), due to climate change and man-made interventions. This poses threats to e.g. reliable intake of fresh water, agriculture and the ecology of these regions. Salt water enters rivers and other waterways through open connections to the sea, thereby forming estuaries where the sea water mixes with the fresh water from the river. Salinization also occurs in coastal aquifers through groundwater flows. Salt intrusion in these systems has been extensively studied and the underlying physical mechanisms are rather well known (Bear et al., 1999; Barlow and Reichard, 2010; MacCready and Geyer, 2010; Geyer and MacCready, 2014). Less attention has been paid to salt intrusion in man-made shipping canals. The latter have been constructed to accommodate transport of goods to harbors that are situated at some distance from the sea, or to shorten trading routes. In this study, the focus is on canals which are separated from the open sea by locks; examples are the North Sea Canal (from the North Sea to Amsterdam, the Netherlands), the Kiel Canal (from the North Sea to the Baltic Sea, Germany), the Boudewijnkanaal (from the North Sea to Brugge, Belgium), and the Ghent-Terneuzen Canal (from the Western Scheldt to the city of Ghent, Belgium).

These man-made canals resemble estuaries, but there are several differences. One of them, which is particularly relevant for salt intrusion, is the presence of locks, that serve to accommodate and control the water level difference between the sea and the canal. Locks obstruct the tides and limit the salt from entering the channel. A second difference concerns the aspect ratio, i.e. width divided by depth, which is usually much smaller in these canals than in natural estuaries. This is a consequence of the fact that morphological processes in natural estuaries tend to form wide and shallow systems (Friedrichs and Aubrey, 1994), while in man-made canals the bathymetry is maintained by anthropogenic measures. The aim is to create a narrow and deep channel, because the depth is the limiting factor for the size of ships. A third difference is that discharge in these canals is often small and controlled by human actions.

Only a few studies have focused on the salt dynamics of man-made canals. Augustijn et al. (2011) found that for the Mark-Vliet river system (the Netherlands), which also has locks at its downstream boundary, discharge is an effective measure to control salinity. Steinhagen et al. (2019) reported that salinity in the Kiel Canal typically

* Corresponding author.
E-mail address: w.t.biemond@uu.nl (B. Biemond).

https://doi.org/10.1016/j.ecss.2024.108654
Received 12 July 2023; Received in revised form 22 January 2024; Accepted 23 January 2024
Available online 24 January 2024

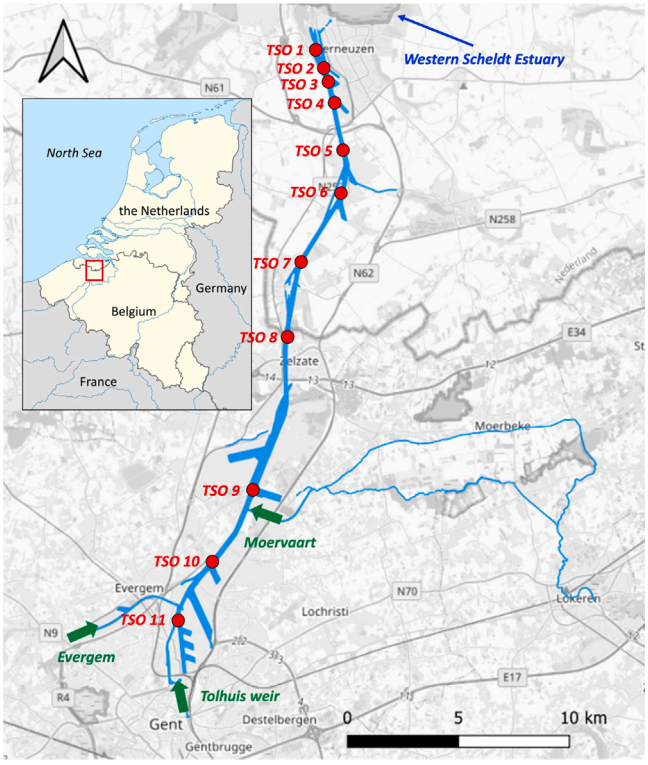

Fig. 1. A map of the Ghent-Terneuzen Canal. The red dots indicate the locations of the TSO measurements.

increases from 3 psu at its connection to the North Sea to 16 psu at the locks near the Baltic Sea, mainly as a consequence of the mean flow direction in this canal. Bertels and Willems (2022) concluded that salinity in the Campine Canal system (Belgium) is increasing due to climate change.

To develop an effective management strategy to prevent salinization of man-made canals, hydrodynamic models are used (Augustijn et al., 2011; Bertels and Willems, 2022; Wijsman, 2013; Verbruggen and van der Baan, 2020). The types of available models range in complexity from simple box models (e.g. Bertels and Willems (2022)) to full-blown three-dimensional numerical models (e.g. Lesser et al., 2004; Shchepetkin and McWilliams, 2005). One-dimensional (1D) models, in which the salt intrusion is described by a simple cross-sectionally averaged advection–diffusion equation, are popular for estuaries (Zhang et al., 2013; Haddout and Maslouhi, 2018), because of their simplicity and because little computational resources are required for model simulations. The skill of this type of model in simulating salinity depends strongly on the formulation of the longitudinal dispersion coefficient $K_{h,1D}$, which parametrizes all the unresolved physics responsible for the salt import. In a 1D model this longitudinal coefficient is equivalent to the effective longitudinal dispersion coefficient $K_{h,eff}$, defined as the dispersion coefficient that represents all down-gradient salt fluxes as a one-dimensional dispersive flux. Observations show that in nature $K_{h,eff}$ is not constant in time and space, but depends on the forcing conditions, local bathymetry and on the flow and salinity field itself (Austin, 2004; Geyer et al., 2008; Díez-Minguito et al., 2013). For estuaries, parametrizations of $K_{h,1D}$ have been presented that are calibrated against observations (Savenije, 2005; Kuijper and Van Rijn, 2011; Gisen et al., 2015). However, for man-made canals, such a calibrated parametrization does not exist, and $K_{h,1D}$ has to be determined by heuristic methods. More knowledge on the dependence of effective longitudinal dispersion in man-made canals on forcing conditions and their consequences for salt intrusion is required to develop a suitable parametrization.

To this end, the overall goal of this study is to better understand salt intrusion and effective longitudinal salt dispersion in man-made canals. A width-averaged (2DV) model will be used to calculate the salt intrusion and effective longitudinal dispersion coefficient. This type of model is appropriate since in man-made canals the main variations in velocity and salinity are expected to occur over the depth. Our specific aims are threefold. The first is to compare the skills of both a calibrated 1D model with constant longitudinal dispersion coefficient $K_{h,1D}$, and a calibrated 2DV model with constant longitudinal dispersion coefficient $K_{h,2D}$. This is done to verify the hypothesis that the 2DV model will perform better, as the assumption of a constant $K_{h,1D}$ does not properly account for salt transport that results from vertical variations in velocity and salinity. The second aim is to understand and quantify how equilibrium and time-dependent responses of salt intrusion and the effective longitudinal dispersion coefficient in these canals depend on forcing conditions, i.e. the discharge and the salinity outside the downstream lock system. The third aim is to find a parametrization for the effective longitudinal dispersion coefficient, which can potentially be used in one-dimensional models. The Ghent-Terneuzen Canal (see Fig. 1) is used as a prototype example. Freshwater discharge in this canal originates from multiple sources around the city of Ghent, indicated with green arrows in Fig. 1: the Moervaart, the locks and weir at Evergem, and the Tolhuis weir. At its downstream boundary in Terneuzen (the Netherlands) a lock complex, which is operated multiple times a day, separates the canal from the Western Scheldt Estuary. The fact that the canal water flows into an estuary results in a fluctuating salinity at the downstream boundary. Detailed salinity measurements in the canal have been done over a multi-year period, and long (multi-yearly) time series for forcing conditions, i.e. discharge and exterior salinity, are available.

Section 2 introduces the available observations in the Ghent-Terneuzen Canal, the one- and two-dimensional models, the formulation and parametrization of the effective longitudinal dispersion coefficient, and the design of the simulations. Section 3 describes the results of the model calibration and simulations. Here, also the performance of the model with the parametrization of $K_{h,1D}$ is assessed. Finally, Section 4 contains a discussion and Section 5 the conclusions.

2. Material and methods

2.1. Field data

Three datasets for the Ghent-Terneuzen Canal were used: exterior salinity, discharge, and salinity inside the canal. The study period spans the years 2014–2021. The data of exterior salinity were obtained by Rijkswaterstaat (the Dutch water agency) with a fixed conductivity–temperature–depth sensor in the outer harbour of Terneuzen at a 10 min interval at two depths. These data were averaged over depth and long-pass filtered in time, to obtain daily depth-averaged salinity values. The data of the discharge were constructed as the sum of the different contributions around Ghent. Flow velocities in the Moervaart were measured with an acoustic Doppler current profiler and multiplied with the cross-section of the channel to obtain the discharges. For the locks at Evergem the discharge was estimated based on the operation of the locks. The largest contribution of the discharge is from the weir at Evergem, where an acoustic discharge meter is employed. Discharge is measured each hour. Discharges from the Tolhuis weir are not measured, but are believed to be small, i.e. lower than 2 $m^3\ s^{-1}$. Furthermore, salinity data measured with a shipborne conductivity–temperature–depth sensor (type YSI EXO-3) at 11 positions in the canal (for locations see Fig. 1) were used for calibration purposes. These measurements were performed by Rijkswaterstaat as part of campaigns that take place about six times a year (https://waterberichtgeving.rws.nl/monitoring/tso-metingen/kanaal-gent-terneuzen). We will refer hereafter to this data as TSO measurements.

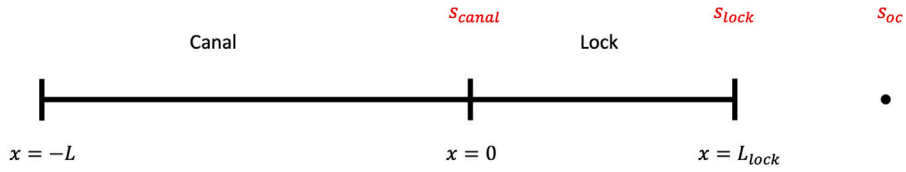

Fig. 2. Sketch of the domain and variables used in the models. Here, $x = -L$ is the upstream boundary, $x = 0$ the downstream boundary of the canal, where the salinity is s_{canal}. The area between $x = 0$ and $x = L_{lock}$ comprises the lock. The salinity s_{lock} is computed from a weighted sum of s_{canal} and the imposed salinity s_{oc} on the outer side of the lock.

2.2. One-dimensional model

The cross-sectionally averaged one-dimensional (1D) model solves the one-dimensional salinity balance (Chatwin and Allen, 1985; Taylor, 1954):

$$\frac{\partial \bar{s}}{\partial t} + \frac{1}{bH}\frac{\partial}{\partial x}\left(bH\left(\bar{u}\bar{s} - K_{h,1D}\frac{\partial \bar{s}}{\partial x}\right)\right) = 0. \tag{1}$$

In this equation, s is salinity and a bar denotes a cross-sectional average, t is time and x is along-channel coordinate, which runs from $x = -L$ to $x = 0$, as is indicated in the model domain sketch in Fig. 2. The horizontal longitudinal dispersion coefficient is denoted by $K_{h,1D}$. The cross-sectionally averaged current $\bar{u} = \frac{Q}{bH}$, where Q is the discharge, H is the depth, and b is the width of the canal. Both H and b are assumed to be constant in the canal. This formulation of the currents assumes that the hydrodynamics are always in equilibrium with the forcing and that variations in the water level of the canal are thus neglected. No salt transport is allowed through the upstream boundary.

To set salinity conditions at the downstream side of the canal $x = 0$, where a lock complex is situated, a parametrization of the salt transport in this structure is required. One way to include the locks is to use a submodel, that takes into account the operation of the locks to calculate the boundary conditions for salinity. However, this approach is cumbersome, as models of salt intrusion through locks are not easily employed, detailed information about the lock operation is required, and in the case of the Ghent-Terneuzen canal there are multiple locks which connect the canal to the Western Scheldt Estuary. Instead, a more pragmatic approach is chosen: comparable to what is done in Biemond et al. (2022), at the downstream side of the canal an extension of the computational domain is added, that serves as a parametrization of the dynamics inside the lock complex. In this additional domain the horizontal coordinate runs from $x = 0$ to $x = L_{lock}$ (see also Fig. 2) and the width of the channel increases exponentially, i.e., $b = b(x = 0)\exp(x/L_b)$, with L_b a given length scale. Eq. (1) is subsequently used to solve for salinity in this domain, where now $K_{h,1D} = K_{h,1D}(x = 0) \cdot \frac{b(x)}{b(x=0)}$, i.e. the longitudinal dispersion coefficient increases exponentially with distance to the canal. To account for the limited exchange induced by the locks, we assume that salinity at $x = L_{lock}$ is given by:

$$s_{lock} = C_{exchange}s_{oc} + (1 - C_{exchange})s_{canal}, \tag{2}$$

where s_{lock} is the salinity value at $x = L_{lock}$, s_{oc} is the prescribed exterior salinity, s_{canal} is the salinity at $x = 0$, and $C_{exchange}$ is an exchange coefficient. To account for the fact that when the discharge is higher, more fresh water will flow through the locks and thus less salt will enter the canal, $C_{exchange}$ is expected to increase when Q decreases, and vice versa. This relation is modeled using a hyperbolic tangent function, which reads

$$C_{exchange}(Q) = \frac{1}{2}(c_1 + c_2) + \frac{1}{2}(c_1 - c_2)\tanh\left(\frac{Q - c_3}{c_4}\right), \tag{3}$$

in which the constants c_1, c_2, c_3 and c_4 are determined through calibration. Quantities c_1 and c_2 are the maximum and minimum value of $C_{exchange}$, respectively. Furthermore, the function is anti-symmetric in Q around c_3 and c_4 controls how sensitive $C_{exchange}$ is to changes in Q. Eq. (1) with boundary conditions Eq. (2) at $x = L_{lock}$ and the no-flux condition at $x = -L$ is numerically solved using central differences for horizontal discretization and a Crank–Nicolson scheme (Crank and Nicolson, 1947) for the time integration.

2.3. Two-dimensional model

The width-averaged two-dimensional (2DV) model consists of equations for flow and salinity that are identical to those presented in Biemond et al. (2022). The difference here is that they are solved on a different domain, viz. that of Fig. 2, with different boundary conditions. Below, only its main characteristics are presented. The horizontal and vertical velocity components for a straight channel are analytical functions of salinity and read

$$\bar{u} = \frac{Q}{bH}, \quad u' = \underbrace{\bar{u}P_1(\tilde{z})}_{u'_Q} + \underbrace{\alpha\frac{d\bar{s}}{dx}P_2(\tilde{z})}_{u'_D}, \quad w = \alpha H\frac{d^2\bar{s}}{dx^2}P_5(\tilde{z}), \quad \text{with} \tag{4}$$

$$P_1(\tilde{z}) = \frac{1}{5} - \frac{3}{5}\tilde{z}^2, \quad P_2(\tilde{z}) = \frac{8}{5} - \frac{54}{5}\tilde{z}^2 - 8\tilde{z}^3, \quad P_5(\tilde{z}) = 2\tilde{z}^4 + \frac{18}{5}\tilde{z}^3 - \frac{8}{5}\tilde{z}.$$

Here, w is vertical velocity, z is the vertical coordinate, $z = 0$ is the mean sea level and $\tilde{z} = \frac{z}{H}$. A bar indicates a cross-sectionally-averaged value and a prime the deviation from this value. The vertical shear associated with $\bar{u}$ is indicated by u'_Q. Parameter $\alpha = \frac{g\beta H^3}{48A_v}$ is a coefficient, and $u'_D = \alpha\frac{d\bar{s}}{dx}P_2(\tilde{z})$ is the density-driven flow, where $g = 9.81$ m s^{-2} is gravitational acceleration, $\beta = 7.6 \cdot 10^{-4}$ g kg^{-1} is the isohaline contraction coefficient and A_v is the constant vertical viscosity coefficient.

For salinity, a two-dimensional advection–diffusion equation is solved, which reads

$$\frac{\partial s}{\partial t} + \frac{1}{b}\frac{\partial}{\partial x}\left(b\left(us - K_{h,2D}\frac{\partial s}{\partial x}\right)\right) + \frac{\partial}{\partial z}\left(ws - K_v\frac{\partial s}{\partial z}\right) = 0, \tag{5}$$

where $K_{h,2D}$ and K_v are the longitudinal and vertical dispersion coefficients, respectively.

The horizontal boundary conditions are identical to those of the 1D model, but additional conditions are needed because of the 2DV configuration. For the vertical profiles of salinity at the upstream boundary $x = -L$ we impose $\frac{\partial s'}{\partial x} = 0$, which prevents formation of a diffusive boundary layer, and at the downstream boundary $x = L_{lock}$ we assume $s' = 0$, which imposes absence of stratification at the ocean boundary, that is at the downstream side of the lock domain. At $x = 0$ we impose continuity of salinity and salt transport. The vertical eddy viscosity A_v, vertical dispersion coefficient K_v and longitudinal dispersion coefficient $K_{h,2D}$ are in Biemond et al. (2022) linked to the amplitude of the tidal current. That is not possible in the man-made canal case, as no tides exist in this system. Sources of dispersion in these systems are wind, shear of velocity and eddies produced by large ships, which are not straightforward to parametrize. We therefore treat these values as calibration parameters.

A formulation for the effective longitudinal dispersion coefficient in the 2DV model is obtained as follows. The cross-sectionally averaged along-channel salt flux F in the 2DV model context reads

$$F = \bar{u}\bar{s} + \overline{u's'} - K_{h,2D}\frac{\partial \bar{s}}{\partial x}, \tag{6}$$

where $\bar{u}\bar{s}$ represents downstream salt flux because of the cross-sectionally averaged current, $\overline{u's'}$ is a down-gradient salt flux induced by the

vertical shear of $\bar{u}$ and the density-driven flow, and $-K_{h,2D}\frac{\partial \bar{s}}{\partial x}$ is the down-gradient salt flux due to longitudinal dispersion. Now, consider the salt flux $\overline{u's'}$ due to the density-driven flow u'_D. As the latter is proportional to salinity gradient $\frac{\partial \bar{s}}{\partial x}$ (see Eq. (4)), it induces a salt flux $-K_{h,d}\frac{\partial \bar{s}}{\partial x}$, where $K_{h,d} = -\alpha\overline{P_2(z)s'}$, the contribution to the effective longitudinal dispersion coefficient from the density-driven flow. The values of $K_{h,d}$ follow from output of the 2DV model. There is also a contribution to the salt flux $\overline{u's'}$ due to u'_Q. As u'_Q is not proportional to the mean salinity gradient, this flux cannot be straightforwardly written as a diffusive flux, and therefore this flux is not considered. This is also justified because $u'_Q \ll u'_D$. All in all, it means that the effective longitudinal dispersion coefficient derived from the 2DV model reads

$$K_{h,eff} = -\alpha\overline{P_2(z)s'} + K_{h,2D}. \tag{7}$$

2.4. Parametrization of the one-dimensional longitudinal dispersion coefficient

A parametrization for $K_{h,1D}$ is constructed from Eq. (7), with the purpose of it to be used in a 1D model. To this end, s' has to be calculated from quantities available in a 1D model. Here, we adopt the relation between the horizontal salinity gradient and the departure of the salinity s' from its depth-averaged value, as is presented in MacCready (2004) in the context of a more simplified, steady model:

$$s' = \frac{H^2}{K_v}\frac{\partial \bar{s}}{\partial x}\left(\bar{u}P_3(\tilde{z}) + \alpha\frac{\partial \bar{s}}{\partial x}P_4(\tilde{z})\right), \quad \text{with} \tag{8}$$

$$P_3(\tilde{z}) = \frac{7}{300} + \frac{1}{10}\tilde{z}^2 - \frac{1}{20}\tilde{z}^4, \quad P_4(\tilde{z}) = -\frac{23}{150} + \frac{4}{5}\tilde{z}^2 - \frac{9}{10}\tilde{z}^4 - \frac{2}{5}\tilde{z}^5.$$

This expression also holds for unsteady conditions, provided that $\frac{\partial s'}{\partial t} \ll u'\frac{\partial \bar{s}}{\partial x}$, for which a justification is given in Appendix A. Moreover, MacCready (2007) also uses Eq. (8) for unsteady conditions. Since our 2DV model is an extension of this model, Eq. (8) is expected to give a first-order approximation of s'. Substitution of Eq. (8) in Eq. (7) yields

$$K_{h,1D} = \frac{\alpha H^2}{K_v}\frac{\partial \bar{s}}{\partial x}\left(0.018\bar{u} + 0.112\alpha\frac{\partial \bar{s}}{\partial x}\right) + K_{h,2D}, \tag{9}$$

which is the proposed parametrization of $K_{h,1D}$ in man-made canals. This expression contains three calibration parameters: A_v, which is contained in α, K_v and $K_{h,2D}$, similar to the 2DV model.

2.5. Design of simulations

Quantification of the differences in skill (regarding salt intrusion) between the 1D model with constant $K_{h,1D}$ and the 2DV model is performed by calibrating both models using the TSO data. For this, the models are forced with observed discharge in Ghent and salinity outside the locks in Terneuzen during the period 2014–2021. The model domain is a straight 27.2 km long channel, 13.5 m deep and 150 m wide. The horizontal step size is 200 m, the number of vertical modes is 10 in the 2DV model, and time steps of one day are used.

To calibrate the models, salinity values are extracted from the models at the times and locations at which observational data are available. We then determine for each model the minimum of a score function, which is defined as the root-mean-squared error between the depth-averaged modeled and measured salinity, while varying the dispersion coefficients and the coefficients of the downstream lock boundary condition. In the 2DV model also the value of the vertical viscosity coefficient is varied. All calibration parameters are assumed to be constant in time and space. The minimum of the score function is found by employing a gradient descent algorithm. Note that in this manner we find different values for both the longitudinal dispersion coefficients and the coefficients of the downstream lock boundary condition of the 1D and 2DV models. The model skill after calibration is quantified by calculating the root-mean-squared error RMSE of the depth-averaged salinity and the normalized root-mean-squared error NRMSE.

Table 1
Values of the calibrated parameters.

Parameter	Unit	1D model	2DV model
Vertical eddy viscosity A_v	$m^2\ s^{-1}$	–	$6.75 \cdot 10^{-4}$
Vertical dispersion coefficient K_v	$m^2\ s^{-1}$	–	$3.07 \cdot 10^{-4}$
Longitudinal dispersion coefficient K_h	$m^2\ s^{-1}$	475	25
Minimum exchange coefficient c_1	–	0.027	0.035
Maximum exchange coefficient c_2	–	0.028	0.042
Coefficient c_3	$m^3\ s^{-1}$	20.2	20
Coefficient c_4	$m^3\ s^{-1}$	4.65	5

To quantify how the salt intrusion and the effective longitudinal dispersion coefficient in man-made canals depend on forcing conditions, equilibrium and time-dependent simulations with the calibrated 2DV model are performed. For the equilibrium simulations, the two forcing parameters, freshwater discharge Q and exterior salinity s_{oc}, are varied over the same range as their observed values in 2014–2021. For each combination of these parameters, the equilibrium salinity field, and from this also the effective longitudinal dispersion coefficient, is determined.

The time-dependent response of salinity in the canal to changes in discharge at the upstream boundary is investigated by performing two simulations, in which we impose a sudden change from a representative value for the winter discharge ($75\ m^3\ s^{-1}$) to a representative value for the summer discharge ($15\ m^3\ s^{-1}$) and vice versa. For exterior salinity, $23\ g\ kg^{-1}$ is used. The time-dependent response to changes in exterior salinity is investigated in the same manner as for changes to discharge. Representative values for exterior salinity in the summer are $28\ g\ kg^{-1}$ and for the winter $18\ g\ kg^{-1}$, while the discharge is $25\ m^3\ s^{-1}$.

The performance of the new parametrization of $K_{h,1D}$ in man-made canals is quantified in the following manner. The parametrization Eq. (9) is implemented in the 1D model. The model is subsequently recalibrated in the same way as the other two models. Afterwards, the longitudinal dispersion coefficient in the 1D model is compared to the effective longitudinal dispersion coefficient in the 2DV model. Finally, the skill of the model in hindcasting the salinity is compared to the 1D model with constant longitudinal dispersion coefficient.

3. Results

3.1. Model calibration

The values for the calibrated dispersion coefficients, eddy viscosity and downstream lock parametrization coefficients for the two models are given in Table 1. The values for A_v and K_v are smaller than those used for estuarine environments, e.g. $A_v = 1.1 \cdot 10^{-3}\ m^2\ s^{-1}$ for the Delaware (MacCready, 2004). This is expected because canal flows are less turbulent than flows in estuaries due to the absence of tides. The fact that $K_{h,2D}$ is small compared to $K_{h,1D}$, indicates that in the 2DV model another process is responsible for the major part of the salt import, which is the density-driven flow (see Eq. (7)). The values of the coefficients of the downstream lock boundary condition imply that in the 1D model the dependence of $C_{exchange}$ on discharge is weak, because the difference between the value of c_1 and c_2 is small. In the 2DV model, this dependence is stronger, and the mean value of $C_{exchange}$ is larger, because the value of c_2 is larger than that of the 1D model. Consequently, in the 2DV model more salt enters the canal through the locks than in the 1D model. The time series of the observed and modeled discharge, exterior salinity and salinity (Fig. 3, see Fig. S2 for a comparison at all the observations points) reveal that the variability of the salinity is fairly well simulated with both models. Compared to the 1D model, the minimum salinity values in winter are better resolved in the 2DV model. It is further visible in Fig S2a that at the measurement point close to the locks, the model underestimates the salinity. This is because the lock parametrization not only represents the flow and salinity in the locks themselves, but also those in a larger

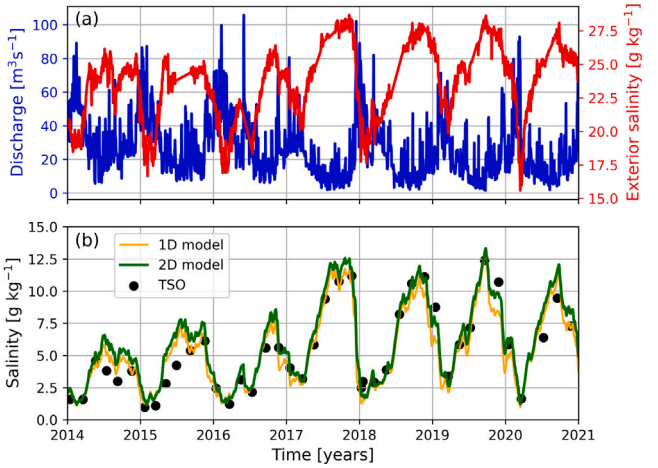

Fig. 3. (a) Observed discharge at Ghent (in blue) and exterior salinity in Terneuzen (in red) versus time. (b) Salinity at 10 km from the downstream boundary in the one-dimensional model (in yellow), in the two-dimensional model (in green) and for the spatially interpolated TSO measurements (black dots), versus time. (For interpretation of the references to color in this figure legend, the reader is referred to the web version of this article.)

area, which also contains the complex bathymetry and flows close to the locks. Regarding the skill of the 1D model, RMSE = 1.20 g kg^{-1} and NMRSE = 0.22, and for the 2DV model RMSE = 0.89 g kg^{-1} and NMRSE = 0.16. The skill of the 2DV model is better than that of the 1D model, indicating that solving for the vertical structure increases the model skill in hindcasting the depth-averaged salinity in the canal.

To visualize to what extent the 2DV model mimics the vertical structure of the salinity field, three examples of salinity contours in the canal from the TSO measurements and the 2DV model are shown in Fig. 4. Panels a and b show a situation in a summer with little salt intrusion, panels c and d show the situation in a winter, and panels e and f the situation in a summer with intense salt intrusion. The observed salinity field has a two-layer structure: a bottom layer, which is characterized by a large vertical gradient in salinity, but a small horizontal gradient, and a surface layer, which has a smaller vertical salinity gradient but a larger horizontal one. Further upstream, the vertical stratification decreases. In panels c and e, close to the bottom near $x = 0$, i.e. the locks in Terneuzen, large salinity values are observed. In the model, the increase of stratification from the surface to mid-depth is well modeled. Also, the values for horizontal salinity gradient in the upper half of the water column compare well with the observations. However, stratification close to the bottom decreases in the model, which is not seen in the observations. This difference does however not lead to large differences in the salinity field in the upper part of the water column, which suggests that the salinity in the bottom layer is only weakly dynamically active.

3.2. Dependence of salinity and effective longitudinal dispersion coefficient on forcing conditions

3.2.1. Sensitivity to discharge and exterior salinity

Fig. 5 displays the sensitivity of equilibrium depth-averaged salinity at two locations in the canal to discharge and exterior salinity. Panels a and b show that the salinity in the canal in most of the parameter space stronger depends on discharge than on exterior salinity. However, high values of discharge are not capable to prevent salt intrusion in the downstream part of the canal if the salinity at the locks is high. For instance, for exterior salinities of 15 g kg^{-1}, a discharge of 30 m^3 s^{-1} is enough to prevent that salt intrusion in the canal exceeds 5 km, but for a exterior salinity of 30 g kg^{-1}, 100 m^3 s^{-1} is required. The salinity upstream in the canal is more sensitive to discharge than

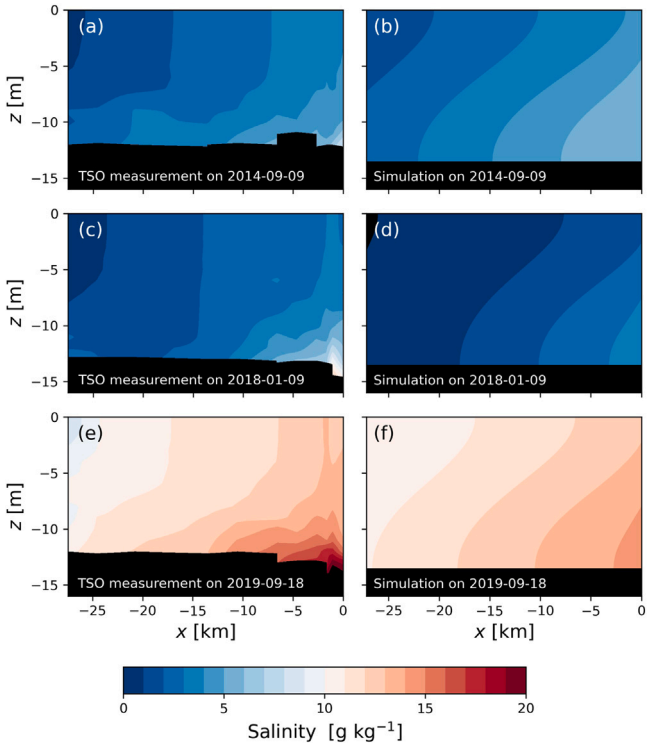

Fig. 4. (a) Observed salinity versus horizontal and vertical coordinate on 2014-09-09. The apparent variation in bed level is caused by measurement cut-offs close to the bottom and does not represent a time-varying bed level. (b) As (a), but as simulated with the two-dimensional model. (c)–(d) As (a)–(b), but on 2018-01-09. (e)–(f) As (a)–(b), but on 2019-09-18.

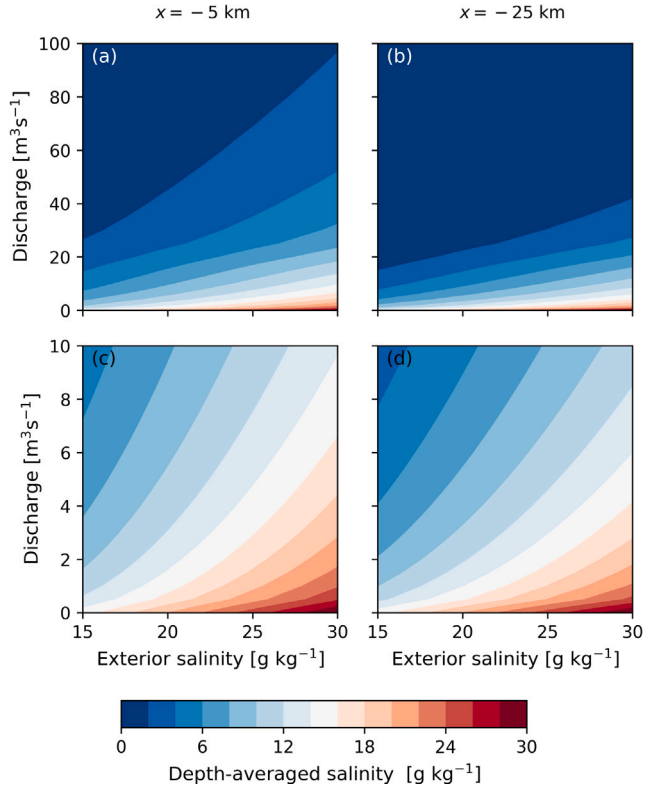

Fig. 5. Depth-averaged salinity from equilibrium simulations versus exterior salinity and discharge. (a) At 5 km from the downstream boundary. (b) At 25 km from the downstream boundary. (c) As (a), but zoomed in on low discharges. (d) As (b), but zoomed in on low discharges.

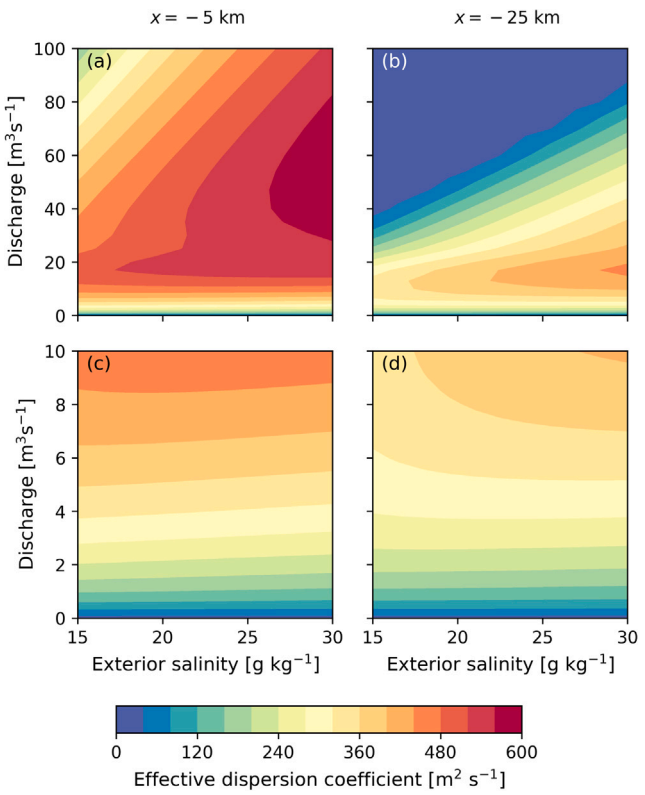

Fig. 6. As Fig. 5, but for the effective longitudinal dispersion coefficient $K_{h,eff}$ instead of depth-averaged salinity.

salinity downstream. A zoom-in for low discharge is presented in panels c and d. It is visible that in this parameter regime, the value of exterior salinity also imposes an important constraint on salinity in the canal.

Regarding the effective longitudinal dispersion coefficient $K_{h,eff}$, it appears that it is small for high discharge and low exterior salinity (Fig. 6). For a larger exterior salinity, $K_{h,eff}$ increases, because horizontal and vertical salinity gradients are larger and thus the dispersion due to density-driven flow becomes stronger. This sensitivity is larger for large discharges, and is almost absent when discharge is low. For high discharges, there is little salt in the canal. This restricts the maximum salinity gradient and thus the effective longitudinal dispersion. In this parameter regime, decreasing discharge is associated with increasing $K_{h,eff}$, because more salt will be present in the canal. However, for low discharges, $K_{h,eff}$ decreases with decreasing discharge, because a smaller discharge decreases the horizontal and vertical salinity gradients in the canal, and thereby $K_{h,eff}$. The separation between the high and low discharge regime is around $Q = 20$ m^3 s^{-1}, but the precise value depends on the location in the canal. Further downstream, $K_{h,eff}$ is always larger, but for low discharge, this difference becomes small.

3.2.2. Response to changes in discharge

The response of the depth-averaged salinity at two locations in the canal to a sudden increase in discharge is shown in Fig. 7a. It takes about 21 days before the downstream point is in equilibrium with the new forcing conditions and 14 days for the upstream point, which becomes completely fresh. The effective longitudinal dispersion $K_{h,eff}$ during this simulation is shown in Fig. 7b. Directly after the change in discharge, $K_{h,eff}$ increases and becomes homogeneous in the entire canal, a feature not captured by the equilibrium simulations (for high discharge). When the salinity in the canal decreases after the change in discharge, $K_{h,eff}$ also decreases, eventually to smaller values than it had before the change in discharge, until equilibrium is reached. Further upstream, $K_{h,eff}$ decreases faster, because this region becomes completely fresh.

In the case of a sudden decrease of fresh water discharge, it turns out (Fig. 7c) that it takes about 60 days before salinity reaches equilibrium in the canal, three times as long as after an increase in discharge. Now the downstream point reaches equilibrium earlier, but the difference is small (4 days) with respect to the total response time. The effective longitudinal dispersion coefficient (panel d) at the downstream location of the canal increases just after the change in discharge, but then decreases again. The increase just after the change is due to the fact that the salt export is suddenly reduced, but the salt import responds slower, which causes an increase in salinity gradients and thus in $K_{h,eff}$. As more salt enters the canal, the salinity gradients and thus $K_{h,eff}$ decrease again. In the upstream part of the canal, $K_{h,eff}$ increases as salt reaches this location, until the salinity gradient is strong enough that the import of salt balances the export of salt by the discharge.

3.2.3. Response to changes in exterior salinity

Fig. 8a shows the response of the salinity to an increase in exterior salinity. It takes a few days before salinity at the upstream point starts to increase after the change at the boundary is imposed. Apart from that, the time evolution of salinity at both locations is similar and both reach equilibrium after about 50 days. The effective longitudinal dispersion coefficient $K_{h,eff}$ (Fig. 8b) rapidly increases in the downstream part of the canal after the increase in exterior salinity, due to the increase of the salinity gradient, and remains almost constant after about a week, while salinity keeps increasing. This indicates that the salinity gradient at this point responds faster to the change in forcing than the salinity itself. Further upstream in the canal, $K_{h,eff}$ increases slower, and reaches equilibrium at the same time as the salinity at this location. Panels c and d of Fig. 8 display the response in salinity and $K_{h,eff}$ to a decrease in exterior salinity. The response time is around 50 days, similar as that for an increase in exterior salinity. The effective longitudinal dispersion coefficient decreases fast at the downstream location, as the salinity gradient is suddenly reduced, but further upstream, its decrease is slower.

3.3. Performance of the parametrization of the effective longitudinal dispersion coefficient

The effective longitudinal dispersion coefficient in the 2DV model for the 2014–2021 simulation is shown in Fig. 9a. Substantial variations in space and time are visible. Values of $K_{h,eff}$ are larger in autumn than in spring, and further downstream. Fig. 9b shows the time-averaged profiles and the standard deviation of $K_{h,eff}$ as a function of x. The variability increases upstream, which is related to the fact that salinity becomes more variable further from the salinity source, and thus variability in effective longitudinal dispersion also increases.

The longitudinal dispersion coefficient in the recalibrated 1D model, using parametrization Eq. (9), is presented in Fig. 9c–d. In most of the domain, a good agreement is found between $K_{h,eff}$ from the 2DV model and $K_{h,1D}$, but the values for $K_{h,1D}$ close to the downstream boundary are larger than those calculated with the 2DV model. This is in line with what is found in Biemond et al. (2022): the MacCready (2004) model overestimates the stratification close to the downstream boundary for high river discharges, which leads to an overestimation of the effective longitudinal dispersion coefficient. However, on the domain scale the difference in effective longitudinal dispersion is small (RMSE = 29.6 m^2 s^{-1}, NMRSE = 0.08), which indicates that this parametrization accounts for the physics of the 2DV model in an appropriate manner.

The error measures for hindcasting the depth-averaged salinity in the canal compared to observations are RMSE = 1.07 g kg^{-1} and a NMRSE = 0.19. These are lower than those of the 1D model with constant eddy diffusion coefficient, indicating that our parametrization of $K_{h,1D}$ improves the performance of the 1D model in simulating salinity in man-made canals.

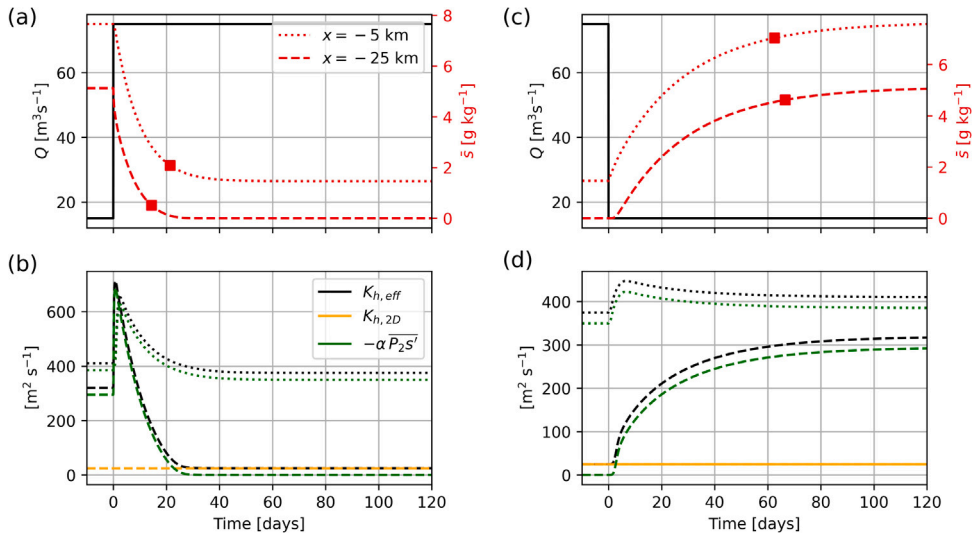

Fig. 7. (a) Discharge (in black) and depth-averaged salinity (in red) at two locations in the canal versus time during an increase in discharge. The red squares indicate where 90% of the total change has passed. (b) As (a), but for the effective longitudinal dispersion coefficient $K_{h,eff}$ (in black), the longitudinal dispersion coefficient $K_{h,2D}$ (in yellow) and the contribution to the effective longitudinal dispersion by the density-driven flow $-\alpha\overline{P_2 s'}$ (see Eq. (7)), in green, at two locations in the canal. (c)–(d) As (a)–(b), but for a decrease in discharge. (For interpretation of the references to color in this figure legend, the reader is referred to the web version of this article.)

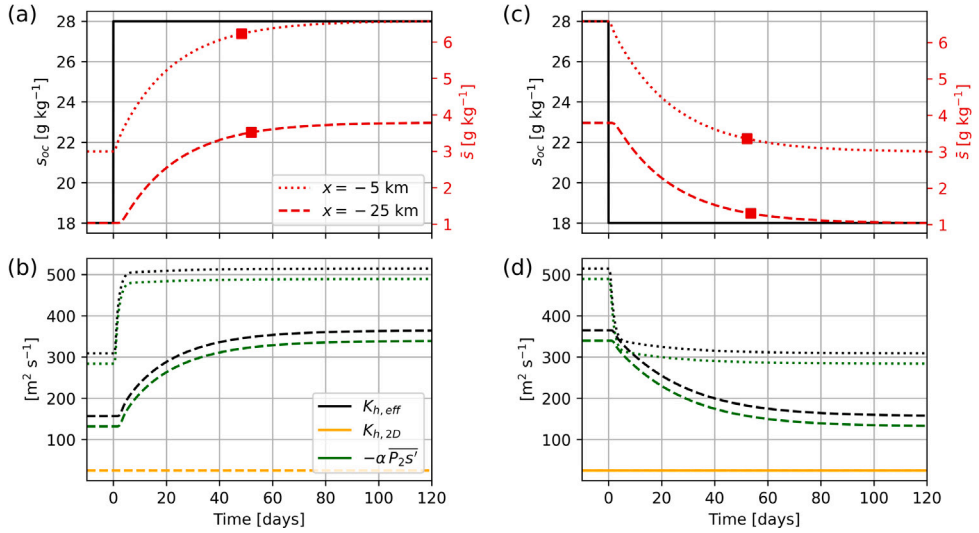

Fig. 8. (a) Exterior salinity (in black) and depth-averaged salinity (in red) at two locations in the canal versus time during an increase of the exterior salinity. (b) As (a), but for the effective longitudinal dispersion coefficient $K_{h,eff}$ (in black), the longitudinal dispersion coefficient $K_{h,2D}$ (in yellow) and the contribution to the effective longitudinal dispersion by the density-driven flow $-\alpha\overline{P_2 s'}$ (see Eq. (7)), in green, at two locations in the canal. (c)–(d) As (a)–(b), but for a decrease in exterior salinity. (For interpretation of the references to color in this figure legend, the reader is referred to the web version of this article.)

4. Discussion

4.1. Main findings and comparison with literature

We have used 1D and 2DV models to study salt intrusion and effective longitudinal dispersion in man-made canals, where the canal from Ghent to Terneuzen was used as a prototype example. When assuming constant viscosity and dispersion coefficients, both models, after calibration, successfully hindcasted the depth-averaged salinities in a multi-year period. However, the skill of the 2DV model is higher than that of the 1D model. This is consistent with our hypothesis, which is that a constant $K_{h,1D}$ cannot properly account for unresolved processes, for example those related to vertical variations of flow and salinity, as the latter depend on the state of the system.

The equilibrium simulations showed that the salt intrusion in canals depends stronger on discharge Q than on exterior salinity s_{oc}. Note however that this conclusion is based on simulations in which the values of both Q and s_{oc} are kept fixed. In reality, Q and s_{oc} vary on a timescale that is shorter than the timescale at which salinity in the canal responds to changes in forcing. Moreover, as Fig. 3 already suggests, Q and s_{oc} are not fully independent. Analysis of the time series reveals that they are anti-correlated at lags between 10 and 80 days (Fig. S1). The largest anti-correlation is at a lag of 45 days (correlation coefficient of −0.43). This means for example that when Q and s_{oc} both have high values, and Q would keep its constant high value, then s_{oc} is expected to decrease after about 10 days. This implies that, for this case, in Figs. 5 and 6 the associated equilibrium state is lower in the diagram.

Lee and Lwiza (2008) found, using regression analysis on salinity time series in Chesapeake Bay, that exterior salinity is more important than discharge for this estuary. The reason for this difference is the low value of the exchange coefficient, which makes that salinity inside the locks s_{lock} only varies between 1.2 and 13.8 g kg^{-1} when s_{oc} varies from 15 to 30 g kg^{-1} and Q is between 10 and 100 m^3 s^{-1}. Regarding the

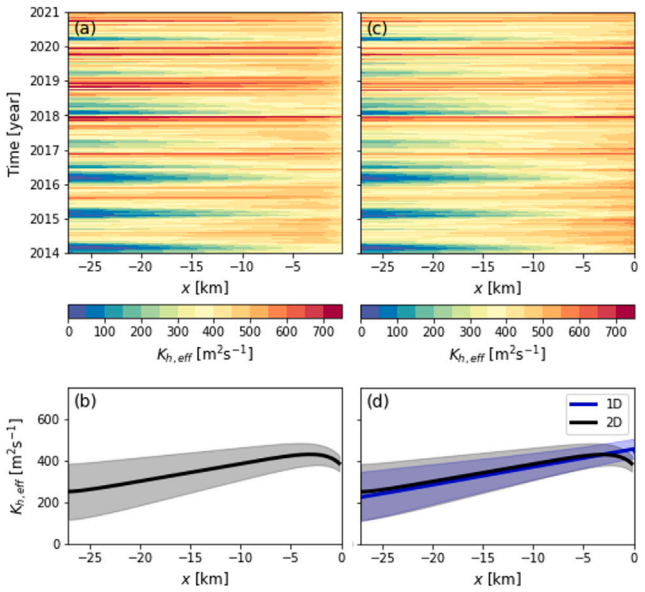

Fig. 9. (a) Effective longitudinal dispersion coefficient $K_{h,eff}$ versus along-channel coordinate and time in the two-dimensional model. (b) Along-channel profile of the time-averaged $K_{h,eff}$ (thick black line) and the standard deviation (shaded area). (c) As (a), but for the effective longitudinal dispersion coefficient in a one-dimensional model simulation using Eq. (9). (d) The blue line indicates the longitudinal profile of $K_{h,eff}$ from a one-dimensional model simulation using Eq. (9) for the longitudinal dispersion coefficient, and the shaded area indicates the standard deviation. The black line is the same as in (b). (For interpretation of the references to color in this figure legend, the reader is referred to the web version of this article.)

longitudinal dispersion coefficient, Augustijn et al. (2011) use a literature value for small streams of 3 m^2 s^{-1} (Kashefipour and Falconer, 2002), which is two orders of magnitude smaller than what we find. This difference is attributed to the fact that they analyze the response of a fresh water body to a sudden intrusion of salt. In this setting, the density-driven circulation is not established yet and hence does not contribute to longitudinal dispersion. The calibration procedure of Bertels and Willems (2022) yields 50–150 m^2 s^{-1} for the Campine Canals, which is a smaller than what we find for the Ghent-Terneuzen Canal. In this case, the depth of their system (5 m versus 13.5 m) is probably responsible for this.

Time-dependent simulations revealed that the response time to changes in discharge is shorter for an increase in discharge than for a decrease, which is a known property of salt intrusion in many estuaries (Chen, 2015; Gong and Shen, 2011; Monismith, 2017). This indicates that the presence of locks does not change this fundamental property of the unsteadiness of salt intrusion. The response times of the canal for an increase or a decrease in exterior salinity are similar. For other coastal water bodies where the exterior salinity fluctuates in comparable magnitudes as in the Ghent-Terneuzen Canal, Flöser et al. (2011) and Lange et al. (2020) have shown that reverse estuarine circulation develops as a response to a decrease in exterior salinity. This is not observed in the Ghent-Terneuzen Canal, due to the low value of the exchange coefficient, which slows down the response. Tests with the 2DV model (not shown) indicates that this reversed circulation occurs when the exchange coefficient would be larger, which also has consequences for the response times.

4.2. Parametrization of longitudinal dispersion

The parametrization that is presented of the effective longitudinal dispersion coefficient, when implemented in the 1D model and after recalibration, is successful in reproducing the effective longitudinal dispersion of the 2DV model in the Ghent-Terneuzen canal. This parametrization is based on approximate analytical solutions of the salt and momentum balances for the flow and vertical salinity profiles that take into account the horizontal salt transport by the density-driven flow, and thus has a solid physical basis. A similar approach can be found in Wei et al. (2016), who used approximate solutions of tidal flow and salinity. Other parametrizations of the longitudinal dispersion coefficient in estuaries (Savenije, 2005; Kuijper and Van Rijn, 2011; Gisen et al., 2015) are based on dimensional analysis of the relevant (mostly tidal) quantities. This precludes a direct comparison between these different formulations, as they are based on dissimilar ways of physical reasoning.

Close to the downstream boundary, the effective longitudinal dispersion coefficient is overestimated by our parametrization. The error originates from a mismatch between the salinity in the 2DV model and the salinity calculated with Eq. (8), which shows the largest difference in the downstream part of the canal (See Fig. S3). To resolve this, a correction to the effective longitudinal dispersion coefficient can be introduced. As vertical advection of salt is the major missing component in the salt balance (Biemond et al., 2022), this is added and the equation we have to solve for s' becomes

$$u'(z)\frac{\partial \bar{s}}{\partial x} + w(z)\frac{\partial s'}{\partial z} = \frac{\partial}{\partial z}\left(K_v \frac{\partial s'}{\partial z}\right). \tag{10}$$

The solution for s' and a calculation of $K_{h,eff}$ are presented in Appendix B. This formulation resolves the effective longitudinal dispersion close to the downstream boundary better. However, solving the 1D advection–diffusion equation with this parametrization of $K_{h,eff}$ using standard numerical techniques, i.e. spatial discretization with central differences and time integration with Crank–Nicholson, appeared to be difficult, because of the extreme sensitivity of $K_{h,1D}$ on the second derivative of the salt field, and therefore this formulation of $K_{h,1D}$ was not implemented.

4.3. Model limitations

Limitations of the 2DV model include the representation of the strongly stratified salinity field in the lower part of the water column in the canal, inclusion of local complex bathymetry and the pragmatic parametrization for salinity at the lock complex at the downstream boundary. The stratification in the lower part of the canal is not well simulated because the vertical viscosity and diffusivity are independent of stratification. Also, unlike in the rest of the canal, close to the locks in Terneuzen the bathymetry is rather complex and the width-averaging procedure in our model is a crude approximation. The model is therefore not capable of accurately representing the physical processes in this part of the domain. These model aspects can be improved, but since their effects are mostly confined to the region close to the downstream locks, and part of these effects are parametrized with Eq. (3), it will not affect our main conclusions. Additionally, our model does not offer the opportunity to study effects of different lock operation strategies on salt intrusion, as lock operation is not included in Eq. (3). For this, a different method to take the locks into account should be applied, but that is beyond the scope of this work.

Our parametrization of the effective longitudinal dispersion coefficient is expected to be successful provided that (1) the channel is sufficiently narrow, i.e. lateral processes can be neglected. Lateral processes occur e.g. when, due to differences in depth, salt intrudes further in the center of the canal than close to the embankments, and the associated lateral density difference induces a horizontal circulation (Lerczak and Geyer, 2004). (2) The width and depth of the channel are approximately constant, and (3) the stratification-turbulence interaction, i.e. the fact that stratification inhibits turbulence, which affects the salt field and thereby stratification (Nunes Vaz et al., 1989; Haas, 1977), is weak. The latter is the case if variations of the Richardson number in time and space are relatively small with respect to its mean value.

4.4. Management strategies

From the model results, the effect of management strategies on salinity in the Ghent-Terneuzen Canal can be estimated. For high discharges ($Q > 20$ m^3 s^{-1}), increasing the discharge is the most effective way to remove the salinity from the canal. For low discharges ($Q < 20$ m^3 s^{-1}), decreasing the exterior salinity, which could be accomplished by limiting the water exchange in the locks or increasing the discharge through the Western Scheldt Estuary, which is less feasible, is also effective. Two specific management strategies are proposed to decrease the salinity of the canal: Firstly, in winter, when large resources of freshwater are available, the discharge through the canal could be increased, in order to reduce salt intrusion in summer. According to the 2DV model, this measure would have an effect up to two months after the increased discharge. This means that in this way it is possible to reduce salinity in the early summer, but that it is not effective in reducing the salinity in late summer, when salt intrusion is usually the most severe. Secondly, when due to rainfall in summer, freshwater is available at the upstream boundary, a 'pulse' of fresh water could be used to flush the canal. The model indicates that about 20 days of increased freshwater discharge are required to reach a new equilibrium. Since the change in salt intrusion length due to an increase in river discharge is to a good approximation linear in time (Biemond et al., 2022), a few days of increased discharge will remove about 10%–20% of the salinity from the canal if the discharge is strong enough. The effect on the salinity field will subsequently remain in the canal for about one to two months, indicating that in this manner it is possible to reduce salinity in the canal in summer. Other specific scenarios could be carried out with the models presented in this study. For this, the 1D model with the new parametrization of the longitudinal dispersion coefficient is the recommended tool, as this model requires less computational resources than the 2DV model, but has a better agreement with the data than the 1D model with a constant longitudinal dispersion coefficient.

There are other options to mitigate salt intrusion, e.g. setting restrictions to the opening time of locks, which limits the water exchange with the exterior water body. In some locks in the Netherlands, e.g. in those of the North Sea Canal bubble screens are employed, to enhance vertical mixing and in this way reduce salt intrusion (Keetels et al., 2011). Here we showed that when freshwater is available, temporary increasing the discharge can also reduce salt intrusion. This may be a more cost-effective management strategy than restricting the lock opening time or the use of a bubble screen. The availability of these instruments to manage salt intrusion means that the effects of climate change (rising sea levels, longer periods of low discharge) in man-made canals can be more effectively mitigated than in estuaries.

5. Conclusions

This study investigated salt intrusion and effective longitudinal salt dispersion in man-made canals. The main findings are that accounting for salt transport by the density-driven current in models is crucial to properly model salinity in man-made canals. Salinity is mostly affected by discharge, while variations in exterior salinity have a smaller effect, because locks limit the water exchange with the external body of water. This indicates that managing the freshwater discharge is an effective measure to control the salinity of man-made canals. The effective longitudinal dispersion coefficient varies an order of magnitude in space and time, i.e. from 25 to 726 m^2 s^{-1}. A new parametrization of the effective longitudinal dispersion coefficient in man-made canals, which is developed using known relations between along-channel quantities and the vertical structure of flow and salinity, captures the variability of the effective longitudinal dispersion coefficient well. This is a promising tool to be used in 1D models for salt intrusion in man-made canals that e.g. account for more sophisticated descriptions of the lock systems.

Open research

Software used for this study will be made available by the authors upon request.

CRediT authorship contribution statement

Bouke Biemond: Writing – original draft, Visualization, Validation, Software, Methodology, Investigation, Formal analysis. **Vincent Vuik:** Resources, Funding acquisition, Data curation. **Paula Lambregts:** Data curation. **Huib E. de Swart:** Writing – review & editing, Supervision, Funding acquisition. **Henk A. Dijkstra:** Writing – review & editing, Supervision, Project administration, Funding acquisition.

Declaration of competing interest

The authors declare that they have no known competing financial interests or personal relationships that could have appeared to influence the work reported in this paper.

Data availability

Data will be made available on request.

Acknowledgments

This work is part of the Perspectief Program SaltiSolutions, which is financed by NWO Domain Applied and Engineering Sciences (2022/TTW/01344701 P18-32 project5) in collaboration with private and public partners. The authors associated with HKV are also funded by the Vlaams-Nederlandse Scheldecommissie. We are grateful to Rijkswaterstaat for providing their data.

Appendix A. Justification that $\frac{\partial s'}{\partial t} \ll u' \frac{\partial \bar{s}}{\partial x}$

We prove that $\frac{\partial s'}{\partial t} \ll u' \frac{\partial \bar{s}}{\partial x}$ by estimation of the magnitude of the two terms. For the first term we use a maximum vertical salinity difference of 10 g kg^{-1}, from Fig. 4, and a response time of one month from Figs. 7 and 8. This gives $\frac{\partial s'}{\partial t} \approx 4 \cdot 10^{-6}$ g kg^{-1}s^{-1}. The magnitude of the second term is estimated as $u' \frac{\partial \bar{s}}{\partial x} \approx \frac{g\beta H^3}{48 A_v} (\frac{\partial \bar{s}}{\partial x})^2$. The magnitude of $\frac{\partial \bar{s}}{\partial x}$ is the average exterior salinity $s_{oc} \approx 20$ g kg^{-1} divided by the length of the canal, which is 27.2 km. Inserting all the numbers gives $u' \frac{\partial \bar{s}}{\partial x} \approx 3 \cdot 10^{-4}$ g kg^{-1}s^{-1}, which is two orders of magnitude larger than $\frac{\partial s'}{\partial t}$.

Appendix B. Derivation of an expression for the effective longitudinal dispersion coefficient with vertical velocity included in the vertical salt balance

In this section, a parametrization for $K_{h,1D}$ is derived, by using a more complex formulation of the vertical salinity profile than what is done in Section 2.4. To this end, Eq. (10) is solved for s', with one modification: the vertical velocity w is multiplied with μ, a factor with a value between 0 and 1, to account for the effect of neglected processes. Note that the old solution can be obtained by setting $\mu = 0$. The new solution will lead to weaker vertical variation of s', because the vertical current transports salt upwards, which, in turn, leads to a weaker effective longitudinal dispersion coefficient, because the term $\overline{u's'}$ in Eq. (7) decreases. This solution for s' reads

$$s'(\tilde{z}) = \frac{H^2}{K_v} \exp(\Psi P_7(\tilde{z})) \cdot \left(c - \bar{u} \frac{\partial \bar{s}}{\partial x} \left(P_{10}(\tilde{z}) - \Psi P_{11}(\tilde{z}) + \frac{1}{2} \Psi^2 P_{12}(\tilde{z}) \right) - \alpha (\frac{\partial \bar{s}}{\partial x})^2 \left(P_{13}(\tilde{z}) - \Psi P_{14}(\tilde{z}) + \frac{1}{2} \Psi^2 P_{15}(\tilde{z}) \right) \right). \quad \text{(B.1)}$$

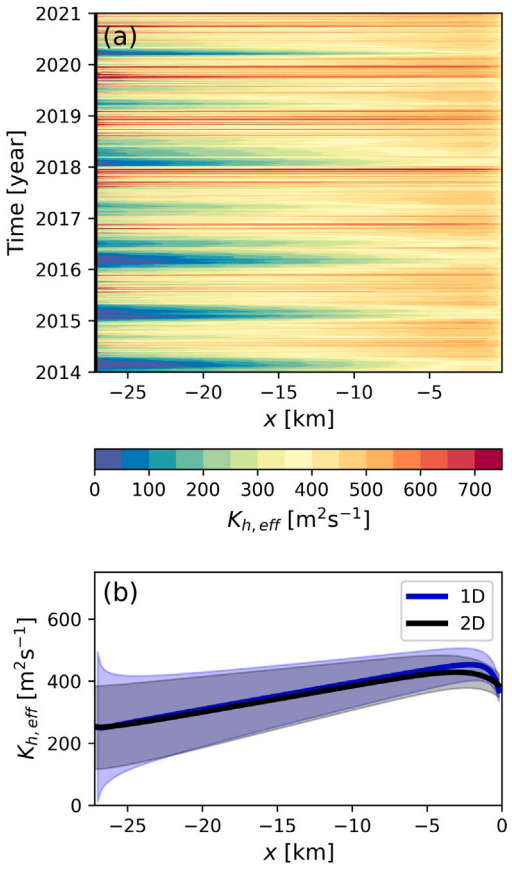

Fig. B.1. As Fig. 9c–d, but the effective longitudinal dispersion coefficient is calculated with Eq. (7), using Eq. (B.1) with $\mu = 0.5$ for s', where the salt field from the 2DV simulation is used for the calculation.

In this equation, c is a constant, chosen such that $\int_{-H}^{0} s' dz = 0$, $\Psi = \frac{\mu\alpha H^2}{K_v}\frac{\partial^2 \bar{s}}{\partial x^2}$ and $P_i(\tilde{z})$, with $i = 10, 11, \ldots 15$, are polynomials. Fig. B.1 shows the effective longitudinal dispersion calculated with Eq. (7), using Eq. (B.1) with $\mu = 0.5$ for s', where the salt field from the 2DV simulation is used for the calculation. This parametrization captures, even without recalibration, the spatio-temporal variability and the along-channel mean value of $K_{h,eff}$ well (RMSE = 43.1 m^2 s^{-1}, NRMSE = 0.12).

To obtain this solution for s', we solve Eq. (10), with the velocities as presented in Eq. (4). As a first step, we integrate Eq. (10) from a depth $z = z'$ to the surface, and apply the boundary conditions at the surface (no flux), which gives

$$\left(\bar{u}H P_6(\tilde{z}) + \alpha H \frac{\partial \bar{s}}{\partial x} P_5(\tilde{z})\right)\frac{\partial \bar{s}}{\partial x} - \mu w(\tilde{z}) s' + K_v \frac{\partial s'}{\partial z} = 0, \tag{B.2}$$

with $P_6(\tilde{z}) = \frac{1}{5}(-\tilde{z} + \tilde{z}^3)$. This is an inhomogeneous ordinary differential equation. To proceed, we find the homogeneous solution s'_{hom}, which reads

$$s'_{hom} = c_1 \exp(\frac{\mu\alpha H^2}{K_v}\frac{\partial^2 \bar{s}}{\partial x^2} P_7(\tilde{z})) = c_1 \exp(\Psi P_7(\tilde{z})), \tag{B.3}$$

where $P_7(\tilde{z}) = -\frac{4}{5}\tilde{z}^2 + \frac{27}{30}\tilde{z}^4 + \frac{2}{5}\tilde{z}^5$. We seek a particular solution by variation of constants. Inserting the homogeneous solution in the inhomogeneous equation, and allowing $c_1 = c_p$ to vary in z, gives

$$\frac{\partial c_p}{\partial z} = -\frac{\bar{u}H}{K_v} P_6(\tilde{z})\frac{\partial \bar{s}}{\partial x}\exp(-\Psi P_7(\tilde{z})) - \frac{\alpha H}{K_v}(\frac{\partial \bar{s}}{\partial x})^2 P_5(\tilde{z})\exp(-\Psi P_7(\tilde{z})). \tag{B.4}$$

No analytical solutions for this equation exist. To proceed, we approximate the exponential with

$$\exp(-\Psi P_7(\tilde{z})) \approx 1 - \Psi P_7(\tilde{z}) + \frac{1}{2}(\Psi P_7(\tilde{z}))^2. \tag{B.5}$$

When using this approximation, we solve Eq. (B.4) by straightforward integration. The result is

$$c_p(\tilde{z}) = -\frac{\bar{u}H^2}{K_v}\frac{\partial \bar{s}}{\partial x}\left(P_{10}(\tilde{z}) - \Psi P_{11}(\tilde{z}) + \frac{1}{2}\Psi^2 P_{12}(\tilde{z})\right) - \frac{\alpha H^2}{K_v}(\frac{\partial \bar{s}}{\partial x})^2\left(P_{13}(\tilde{z}) - \Psi P_{14}(\tilde{z}) + \frac{1}{2}\Psi^2 P_{15}(\tilde{z})\right), \tag{B.6}$$

where

$$P_{10}(\tilde{z}) = \int P_6(\tilde{z}) d\tilde{z}, \quad P_{11}(\tilde{z}) = \int P_6(\tilde{z}) P_7(\tilde{z}) d\tilde{z},$$
$$P_{12}(\tilde{z}) = \int P_6(\tilde{z}) P_7(\tilde{z})^2 d\tilde{z}, \quad P_{13}(\tilde{z}) = \int P_5(\tilde{z}) d\tilde{z},$$
$$P_{14}(\tilde{z}) = \int P_5(\tilde{z}) P_7(\tilde{z}) d\tilde{z}, \quad P_{15}(\tilde{z}) = \int P_5(\tilde{z}) P_7(\tilde{z})^2 d\tilde{z}.$$

The total solution is found by adding the homogeneous solution and the particular solution and is presented in Eq. (B.1).

Appendix C. Supplementary data

Supplementary material related to this article can be found online at https://doi.org/10.1016/j.ecss.2024.108654.

References

Augustijn, D.C.M., van den Berg, M., de Bruine, E., Korving, H., 2011. Dynamic control of salt intrusion in the Mark-Vliet river system, the Netherlands. Water Resour. Manag. 25 (3), 1005–1020. http://dx.doi.org/10.1007/s11269-010-9738-1.

Austin, J.A., 2004. Estimating effective longitudinal dispersion in the Chesapeake Bay. Estuar. Coast. Shelf Sci. 60 (3), 359–368. http://dx.doi.org/10.1016/j.ecss.2004.01.012.

Barlow, P.M., Reichard, E.G., 2010. Saltwater intrusion in coastal regions of North America. Hydrogeol. J. 18 (1), 247. http://dx.doi.org/10.1007/s10040-009-0514-3.

Bear, J., Cheng, A.H.D., Sorek, S., Ouazar, D., Herrera, I., 1999. Seawater Intrusion in Coastal Aquifers: Concepts, Methods and Practices, vol. 14, Springer Science & Business Media.

Bellafiore, D., Ferrarin, C., Maicu, F., Manfè, G., Lorenzetti, G., Umgiesser, G., Zaggia, L., Levinson, A.V., 2021. Saltwater intrusion in a Mediterranean delta under a changing climate. J. Geophys. Res.: Oceans 126 (2), http://dx.doi.org/10.1029/2020JC016437.

Bertels, D., Willems, P., 2022. Climate change impact on salinization of drinking water inlets along the Campine Canals, Belgium. J. Hydrol. Regional Stud. 42, 101129. http://dx.doi.org/10.1016/j.ejrh.2022.101129.

Biemond, B., de Swart, H.E., Dijkstra, H.A., Díez-Minguito, M., 2022. Estuarine salinity response to freshwater pulses. J. Geophys. Res.: Oceans 127 (11), e2022JC018669. http://dx.doi.org/10.1029/2022JC018669.

Chatwin, P., Allen, C., 1985. Mathematical models of dispersion in rivers and estuaries. Annu. Rev. Fluid Mech. 17 (1), 119–149. http://dx.doi.org/10.1146/annurev.fl.17.010185.001003.

Chen, S.N., 2015. Asymmetric estuarine responses to changes in river forcing: A consequence of nonlinear salt flux. J. Phys. Oceanogr. 45 (11), 2836–2847. http://dx.doi.org/10.1175/JPO-D-15-0085.1.

Crank, J., Nicolson, P., 1947. A practical method for numerical evaluation of solutions of partial differential equations of the heat-conduction type. In: Mathematical Proceedings of the Cambridge Philosophical Society, vol. 43, (no. 1), Cambridge University Press, pp. 50–67. http://dx.doi.org/10.1017/S0305004100023197.

Díez-Minguito, M., Contreras, E., Polo, M., Losada, M., 2013. Spatio-temporal distribution, along-channel transport, and post-riverflood recovery of salinity in the Guadalquivir Estuary (SW Spain) . J. Geophys. Res.: Oceans 118 (5), 2267–2278. http://dx.doi.org/10.1002/JGRC.20172.

Eslami, S., Hoekstra, P., Minderhoud, P.S.J., Trung, N.N., Hoch, J.M., Sutanudjaja, E.H., Dung, D.D., Tho, T.Q., Voepel, H.E., Woillez, M.-N., van der Vegt, M., 2021. Projections of salt intrusion in a mega-delta under climatic and anthropogenic stressors. Communi. Earth Environ. 2 (1), 142. http://dx.doi.org/10.1038/s43247-021-00208-5.

Flöser, G., Burchard, H., Riethmüller, R., 2011. Observational evidence for estuarine circulation in the German Wadden Sea. Cont. Shelf Res. 31 (16), 1633–1639. http://dx.doi.org/10.1016/j.csr.2011.03.014.

Friedrichs, C.T., Aubrey, D.G., 1994. Tidal propagation in strongly convergent channels. J. Geophys. Res.: Oceans 99 (C2), 3321–3336. http://dx.doi.org/10.1029/93JC03219.

Geyer, W.R., Chant, R., Houghton, R., 2008. Tidal and spring-neap variations in horizontal dispersion in a partially mixed estuary. J. Geophys. Res.: Oceans 113 (C7), http://dx.doi.org/10.1029/2007JC004644.

Geyer, W.R., MacCready, P., 2014. The estuarine circulation. Annu. Rev. Fluid Mech. 46, 175–197. http://dx.doi.org/10.1146/annurev-fluid-010313-141302.

Gisen, J., Savenije, H., Nijzink, R., 2015. Revised predictive equations for salt intrusion modelling in estuaries. Hydrol. Earth Syst. Sci. 19 (6), 2791–2803. http://dx.doi.org/10.5194/hess-19-2791-2015.

Gong, W., Shen, J., 2011. The response of salt intrusion to changes in river discharge and tidal mixing during the dry season in the Modaomen Estuary, China. Cont. Shelf Res. 31 (7–8), 769–788. http://dx.doi.org/10.1016/j.csr.2011.01.011.

Haas, L.W., 1977. The effect of the spring-neap tidal cycle on the vertical salinity structure of the James, York and Rappahannock Rivers, Virginia, U.S.A.. Estuar. Coast. Mar. Sci. 5 (4), 485–496. http://dx.doi.org/10.1016/0302-3524(77)90096-2.

Haddout, S., Maslouhi, A., 2018. One-dimensional hydraulic analysis of the effect of sea level rise on salinity intrusion in the Sebou Estuary, Morocco. Marine Geodesy 41 (3), 270–288. http://dx.doi.org/10.1080/01490419.2017.1420713.

Kashefipour, S.M., Falconer, R.A., 2002. Longitudinal dispersion coefficients in natural channels. Water Res. 36 (6), 1596–1608. http://dx.doi.org/10.1016/S0043-1354(01)00351-7.

Keetels, G., Uittenbogaard, R., Cornelisse, J., Villars, N., Pagee, H.V., 2011. Field study and supporting analysis of air curtains and other measures to reduce salinity transport through shipping locks. Irrigation Drainage 60 (S1), 42–50. http://dx.doi.org/10.1002/ird.679.

Kuijper, K., Van Rijn, L.C., 2011. Analytical and numerical analysis of tides and salinities in estuaries; part II: salinity distributions in prismatic and convergent tidal channels. Ocean Dyn. 61, 1743–1765. http://dx.doi.org/10.1007/s10236-011-0454-z.

Lange, X., Klingbeil, K., Burchard, H., 2020. Inversions of estuarine circulation are frequent in a weakly Tidal Estuary with variable wind forcing and seaward salinity fluctuations. J. Geophys. Res.: Oceans 125 (9), e2019JC015789. http://dx.doi.org/10.1029/2019JC015789.

Lee, Y.J., Lwiza, K.M., 2008. Factors driving bottom salinity variability in the Chesapeake Bay. Cont. Shelf Res. 28 (10), 1352–1362. http://dx.doi.org/10.1016/j.csr.2008.03.016.

Lerczak, J.A., Geyer, W.R., 2004. Modeling the lateral circulation in straight, stratified estuaries. J. Phys. Oceanogr. 34 (6), 1410–1428. http://dx.doi.org/10.1175/1520-0485(2004)034<1410:MTLCIS>2.0.CO;2.

Lesser, G.R., Roelvink, J.v., van Kester, J.T.M., Stelling, G., 2004. Development and validation of a three-dimensional morphological model. Coast. Eng. 51 (8–9), 883–915. http://dx.doi.org/10.1016/j.coastaleng.2004.07.014.

MacCready, P., 2004. Toward a unified theory of tidally-averaged estuarine salinity structure. Estuaries 27 (4), 561–570. http://dx.doi.org/10.1007/BF02907644.

MacCready, P., 2007. Estuarine adjustment. J. Phys. Oceanogr. 37 (8), 2133–2145. http://dx.doi.org/10.1175/JPO3082.1.

MacCready, P., Geyer, W.R., 2010. Advances in estuarine physics. Ann. Rev. Mar. Sci. 2 (1), 35–58. http://dx.doi.org/10.1146/annurev-marine-120308-081015.

Monismith, S., 2017. An integral model of unsteady salinity intrusion in estuaries. J. Hydraul. Res. 55 (3), 392–408. http://dx.doi.org/10.1080/00221686.2016.1274682.

Nunes Vaz, R.A., Lennon, G.W., de Silva Samarasinghe, J.R., 1989. The negative role of turbulence in estuarine mass transport. Estuar. Coast. Shelf Sci. 28 (4), 361–377. http://dx.doi.org/10.1016/0272-7714(89)90085-1.

Savenije, H.H., 2005. Salinity and Tides in Alluvial Estuaries. Gulf Professional Publishing.

Shchepetkin, A.F., McWilliams, J.C., 2005. The regional oceanic modeling system (ROMS): a split-explicit, free-surface, topography-following-coordinate oceanic model. Ocean Model. 9 (4), 347–404. http://dx.doi.org/10.1016/j.ocemod.2004.08.002.

Steinhagen, S., Karez, R., Weinberger, F., 2019. Surveying seaweeds from the Ulvales and Fucales in the world's most frequently used artificial waterway, the Kiel Canal. Botanica Marina 62 (1), 51–61. http://dx.doi.org/10.1515/bot-2018-0020.

Taylor, G.I., 1954. The dispersion of matter in turbulent flow through a pipe. Proc. R. Soc. Lond. Ser. A. Math. Phys. Sci. 223 (1155), 446–468. http://dx.doi.org/10.1098/rspa.1954.0130.

Verbruggen, W., van der Baan, J., 2020. Ontwikkeling zesde-generatie 3D Noordzeekanaal AmsterdamRijnkanaal model: Modelbouw, kalibratie en validatie. Technical Report, Deltares, URL https://publications.deltares.nl/11205258_011.pdf (in Dutch).

Wei, X., Schramkowski, G.P., Schuttelaars, H.M., 2016. Salt dynamics in well-mixed estuaries: importance of advection by tides. J. Phys. Oceanogr. 46 (5), 1457–1475. http://dx.doi.org/10.1175/JPO-D-15-0045.1.

Wijsman, J.W.M., 2013. Panama Canal Extension: A Review on Salt Intrusion into Gatun Lake. Technical Report, IMARES, URL https://library.wur.nl/WebQuery/wurpubs/fulltext/288785.

Zhang, W., Feng, H., Zheng, J., Hoitink, A., van der Vegt, M., Zhu, Y., Cai, H., 2013. Numerical simulation and analysis of saltwater intrusion lengths in the Pearl River Delta, China. J. Coast. Res. 29 (2), 372–382. http://dx.doi.org/10.2112/JCOASTRES-D-12-00068.1.